

# Integrating Metalens Modeling into Multiscale Optical System Simulations

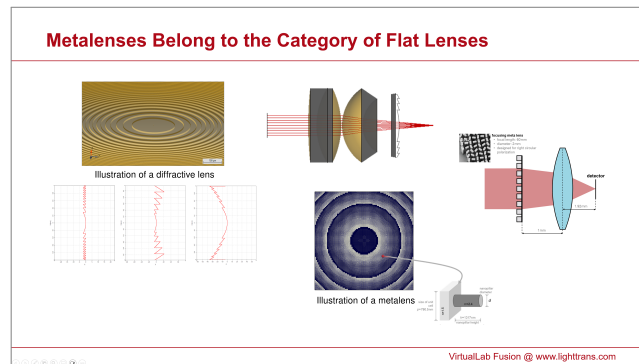
Frank Wyrowski

November 2024

## Abstract

This paper explores the topic of metalenses, which has recently gained considerable attention. Metalenses are a distinct class of flat lenses, alongside diffractive and Fresnel lenses. We present the concepts and showcase the capabilities of VirtualLab Fusion software for simulating and designing metalenses. The techniques and features introduced are scheduled to be released in 2025. Reach out to [support@lighttrans.com](mailto:support@lighttrans.com) for additional release details and any inquiries you may have concerning metalens design and modeling.

This paper derives from the transcript and slides of the webinar "Let's Talk About Metalenses," presented by Frank Wyrowski at the Photonics Media webinar on May 29, 2024. Consult the slides.pdf file to view all slide images.



# 1 Introduction

## Slides #4–5

At LightTrans International, we create the VirtualLab Fusion optics software and distribute it worldwide through our network of distributors. **VirtualLab Fusion serves as a multiscale optical simulation platform** developed to manage a wide variety of optics and photonics applications, with flat lenses being just one example. This paper highlights the potential of VirtualLab Fusion in the field of flat lenses. As software developers, it is our responsibility to offer our continuously expanding customer base robust design and modeling tools to assess and implement metalenses and other flat lenses in practical applications. In this article, we explore certain tasks and challenges faced during the integration of flat lenses into the modeling and design of lens systems in software development.

## Slides #6–7

Given that optics software relies on precise and reliable simulation models, it is essential for us as developers to thoroughly explore the subject and gain a comprehensive understanding of the fundamental physics. This inevitably brings us to some mathematical analyses and equations, which are essential for a serious discussion. However, because these mathematical techniques will be integrated into VirtualLab Fusion, users engaged in practical tasks with VirtualLab Fusion are not required to possess detailed knowledge of the fundamental physics involved. Alongside an exploration of theoretical concepts, this paper will include various example simulations and designs.

In wrapping up the introductory remarks, we would like to stress that at LightTrans International, we maintain an unbiased stance regarding the significance of flat lenses. Our mission is to equip you with robust software tools that enable you to investigate the significance and use of flat lens technology in your work.

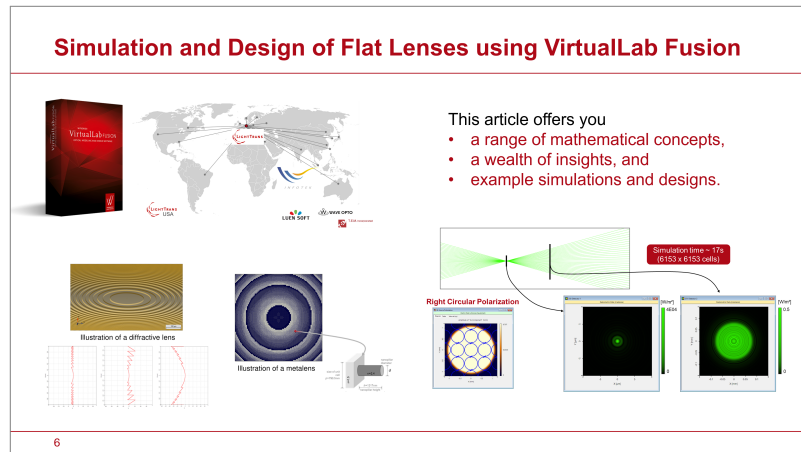


Figure 1: Slide #6

## 2 Multiscale Optical Simulation

### Slides #9–10

Metasurfaces employ nanostructures with a high refractive index, commonly known as meta-atoms or metacells, arranged on a substrate that has a lower refractive index. This approach has been recognized for a while [2], but it has recently gained renewed interest [3]. For an initial insightful read, consult the review authored by Lalanne and Chavel [4]. In addition, the informative tutorial by Yang Fan et al. is recommended, which includes numerous additional references [6].

### Slides #11–12

Given that metasurfaces are composed of nanostructures, it is clear that a geometrical optics approach is unsuitable. Instead, it is necessary to utilize electromagnetic field theory based on Maxwell's equations, commonly known as physical optics. Thus, incorporating metalenses or other flat lenses into a lens system, together with conventional lens surfaces and other components, creates a multiscale system. This requires an approach to optical modeling that spans multiple scales, often referred to as **multiscale optical simulation**. To put it plainly and emphatically: achieving multiscale simulation is not possible by linking various optics software tools through data interfaces. Rather, a comprehensive strategy is required, grounded in a sophisticated formulation of the physical optics foundation for optics software. Modeling optical systems across different scales requires the **integration of many and diverse simulation models within a unified physical optics framework**. This is the approach that we take with our VirtualLab Fusion software.

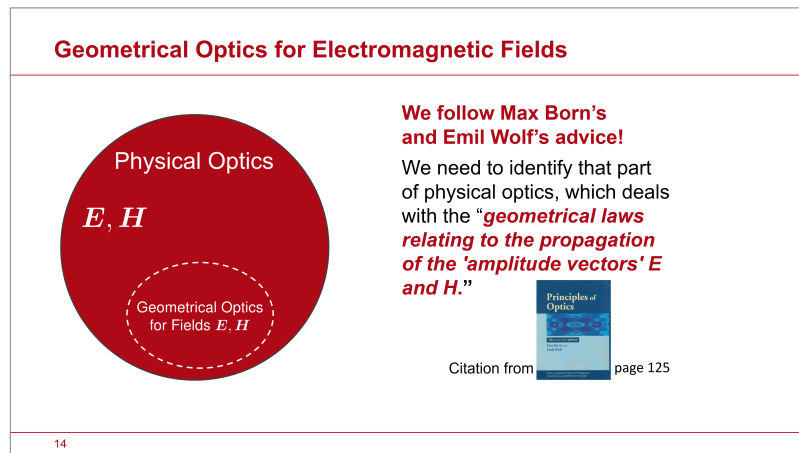


Figure 2: Slide #14

### Slides #13–15

Among various other technological innovations in VirtualLab Fusion, the advancement of geometrical optics for electromagnetic fields enables its smooth incorporation with other physical optics simulation techniques. To achieve this, we adhered to the

guidance provided several decades ago by Max Born and Emil Wolf [1]. They strongly advised expanding the foundations of geometrical optics to include electromagnetic fields. By employing our unified approach for multiscale simulation, we can seamlessly link the geometrical optics modeling of a traditional lens surface with the sophisticated simulation model for a metalens. This leads to unparalleled speed in multiscale simulation when utilizing VirtualLab Fusion.

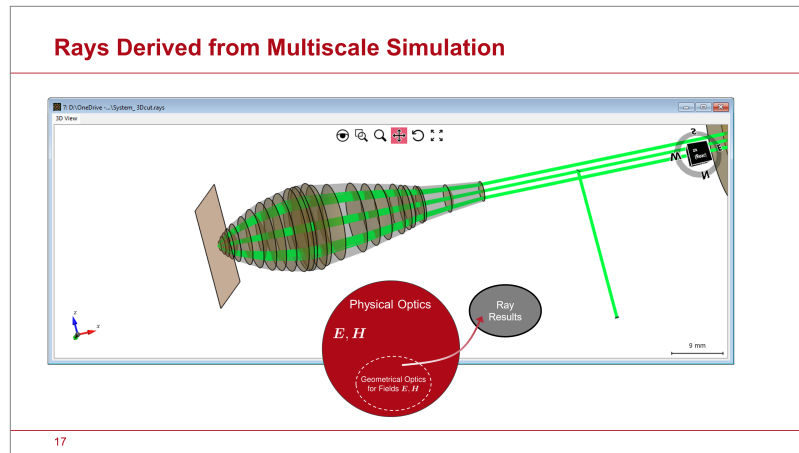


Figure 3: Slide #17

### Slides #16–21

An illustrative scenario for wafer inspection demonstrates the application of multiscale simulation using VirtualLab Fusion. The simulation models for lenses and a grating are connected in a non-sequential multiscale simulation. Although this simulation is entirely based on a physical-optics framework, it conveniently provides access to ray data. Ray data are derived from the subset of geometrical optics for electromagnetic fields within the physical optics framework. In the focal region, the light strikes the wafer structure and the reflected light travels back through the lens system to form the image. The outcome is illustrated for the wafer positioned precisely in the focal plane and also when the wafer is slightly displaced from the focus. The simulation time is a few seconds on a standard laptop. As demonstrated in this example, VirtualLab Fusion enables fast modeling of multiscale systems by connecting different simulation models.

### Slide #22

The primary challenge in integrating metalenses into the multiscale simulation framework of VirtualLab Fusion is creating a metalens simulation model that can seamlessly interact with the simulation models of other components, such as traditional lenses. Before we explore our approach to addressing this challenge, we address the question: What are the expected results of integrating flat lenses into optical design?

### 3 Application Potential of Flat Lenses

#### Slides #24–29

To address this question, we present some basic observations. To generate the image of an object point, such as the axial object point, we design a suitable surface. Replacing this surface with a flat lens does not alter the distances to the object and image planes. As a result, flattening the lens does not decrease the length of the system. Next, we add another object point, which requires a distinct surface for accurate imaging. A single surface cannot accurately image multiple object points. Therefore, adding more surfaces to correct aberrations is crucial, a concept well recognized in lens design. There is no evidence to suggest that flat lenses eliminate this requirement. To gain further insight, we consider the design of a beam expander. In this case, an initial lens is necessary to transform the incoming planar phase into either a converging or diverging spherical phase. The divergent case is demonstrated. A second lens is utilized to collimate the incoming light. Thus, the use of two lenses is necessary. The degree of beam expansion is governed by the distance  $d$  between the lenses and their numerical apertures. Flattening the lenses does not change that outcome.

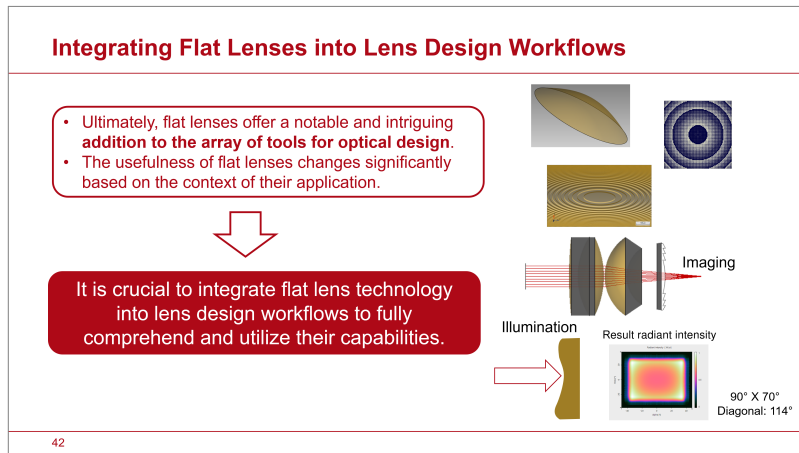


Figure 4: Slide #42

#### Slides #30–40

Based on these observations and additional factors, we arrive at the following conclusions. Flat lenses reduce both the thickness and weight of the lenses. The thin design of flat lenses allows for more possibilities in reducing the distance between lens surfaces. The thickness of conventional lens surfaces limits how close they can be placed to each other. This restriction is removed when using flat lenses. The fabrication methods for flat lenses vary from those for traditional lenses, which may offer benefits in specific scenarios. Flat lenses could provide new opportunities for switchable lenses. Replacing thick lens surfaces with flat surfaces changes the aberration dynamics in the system, which may enhance aberration correction possibilities based

on the particular scenario. Employing diffractive lenses, which exhibit strong and opposing chromatic aberrations, to counteract the chromatic aberrations of smooth lens surfaces serves as a well-documented instance of this potential. Some characteristics of flat lenses, such as its polarization-sensitive function, may be considered beneficial or detrimental depending on their use. Later in this article, we present an example that illustrates the application of polarization sensitivity. Considering these observations, there is no indication that flat lenses, including metalenses, decrease the overall length of the system or the number of lens surfaces in optical systems beyond the capabilities of aspherical and freeform surfaces.

#### Slides #41–42

This implies that the slim profile of flat lenses is the key factor in their potential for miniaturization. Nothing more, nothing less. Ultimately, flat lenses offer a notable and intriguing addition to the array of tools for optical design. The usefulness of flat lenses changes significantly based on the context of their application. In conclusion, it is crucial to integrate flat lens technology into lens design workflows to fully comprehend and utilize their capabilities. It is time to practically evaluate the potential of flat lenses and move beyond mere theoretical debates.

As mentioned before, the primary challenge in integrating metalenses into a multi-scale modeling framework is creating a metalens simulation model that can seamlessly interact with the simulation models of other components, such as traditional lenses. Next, we will explore the solution to this challenge.

## 4 Interoperable Simulation Model for Metalenses

#### Slide #44

Lens systems convert wavefronts originating from object points into wavefronts that create the image points. Wavefronts are mathematically represented by their corresponding phase function  $\psi(\mathbf{r})$ , which we call the **wavefront phase**. The wavefront phase is of pivotal importance in both the design and simulation of lens systems.

#### Slide #45

In geometrical optics, the wavefront phase is directly connected to the local ray direction vector  $\hat{\mathbf{s}}$  through the equation

$$\hat{\mathbf{s}}_{\perp}(\mathbf{r}) = \frac{\{\nabla_{\perp}\psi\}(\mathbf{r})}{k_0 n} \quad (1)$$

where  $\perp$  represents the x and y components, and  $s_z$  is determined by  $\|\hat{\mathbf{s}}\| = 1$ .

#### Slide #46

**In physical optics, the wavefront phase retains its crucial significance.** It is now integrated into the electric field vector  $\mathbf{E}(\mathbf{r})$  through

$$\mathbf{E}(\mathbf{r}) = \mathbf{U}(\mathbf{r}) \exp[i\psi(\mathbf{r})] \quad (2)$$

with

$$U_\ell(\mathbf{r}) := |E_\ell(\mathbf{r})| \exp[i \arg U_\ell(\mathbf{r})] \quad (3)$$

for the components  $\ell = x, y, z$ . In multiscale optics simulations,  $\psi$  is utilized as a continuous and smooth phase that is shared across all components. The electric field components can possess extra phases  $\arg U_\ell$ , such as a vortex associated with an angular momentum beam.

**Slide #47**

For instance, the phase of a Gaussian-Laguerre (0,1) beam after propagation can be broken down into a spherical wavefront phase and a phase dislocation. The separation of the wavefront phase from other phase contributions of the electric field components is one of several concepts that endow VirtualLab Fusion with its exceptional lens modeling capabilities.

**Slide #48**

Next, we examine the manner in which a lens alters the wavefront phase. Conventional lenses modify the wavefront phase through the optical path length (OPL) between their surfaces. The phase is derived from the OPL through

$$\psi = k_0 \text{OPL}. \quad (4)$$

This outcome is equally valid in the realm of physical optics. The resulting phase is continuous and is not expressed as modulo  $2\pi$ , which means that it is unwrapped. The variation in the wavefront phase  $\psi$  is independent of the polarization of the electric field! From a simulation perspective, this represents a highly relaxed numerical scenario.

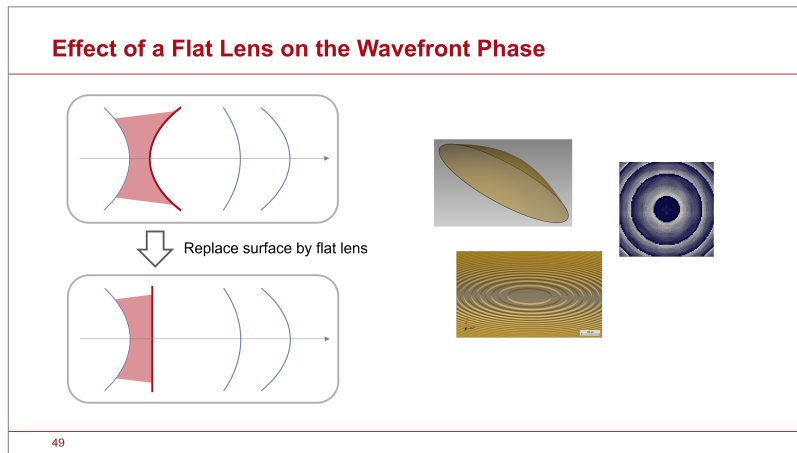


Figure 5: Slide #49

**Slides #49–52**

We now consider the scenario involving a flat lens. The influence of the flat lens on

the field at any location on its planar surface can be characterized by

$$\mathbf{E}_{\perp}^{\text{out}} = \mathbf{M}\mathbf{E}_{\perp}^{\text{in}}, \quad (5)$$

with  $\mathbf{E}_{\perp} = (E_x, E_y)$  and the quadratic matrix

$$\mathbf{M} = \begin{pmatrix} M_{xx} & M_{xy} \\ M_{yx} & M_{yy} \end{pmatrix}. \quad (6)$$

In the subsequent discussion, the z-component of the field is irrelevant, and for the sake of simplicity, we omit the  $\perp$  symbol. The values of the matrix  $\mathbf{M}$  can be obtained using any suitable simulation model of the flat lens surface. Specific decisions regarding the surface structure and the flat lens and an appropriate simulation model for  $\mathbf{M}$  will be addressed later in this article. Now we concentrate on the effect of the flat lens on the wavefront phase of the incoming field. The subsequent analysis of the impact of a flat lens on the wavefront phase applies to any kind of flat lens and to the simulation model chosen for the matrix  $\mathbf{M}$ . Thus, we proceed with this analysis.

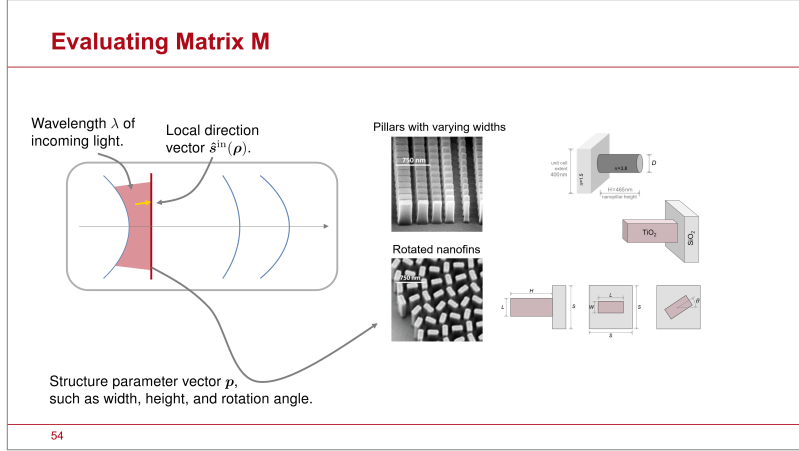


Figure 6: Slide #54

### Slide #53

The wavefront phase  $\psi^{\text{in}}$  of the incoming field, can be explicitly separated from the matrix multiplication, leading to the expression

$$\mathbf{E}^{\text{out}} = \mathbf{U}^{\text{out}} \exp[i\psi^{\text{out}}] = (\mathbf{M}\mathbf{U}^{\text{in}}) \exp[i\psi^{\text{in}}]. \quad (7)$$

where

$$\psi^{\text{out}} = \psi^{\text{in}} + \Psi. \quad (8)$$

The phase  $\Psi$  represents the change in the wavefront phase of the input due to the flat lens. In the case of flat lenses, the phase  $\Psi$  is not determined by an OPL between the lens surfaces, but must be derived from the matrix effect on the input field, represented as  $\mathbf{M}\mathbf{U}^{\text{in}}$ . Given the critical importance of the phase  $\Psi$  in lens modeling

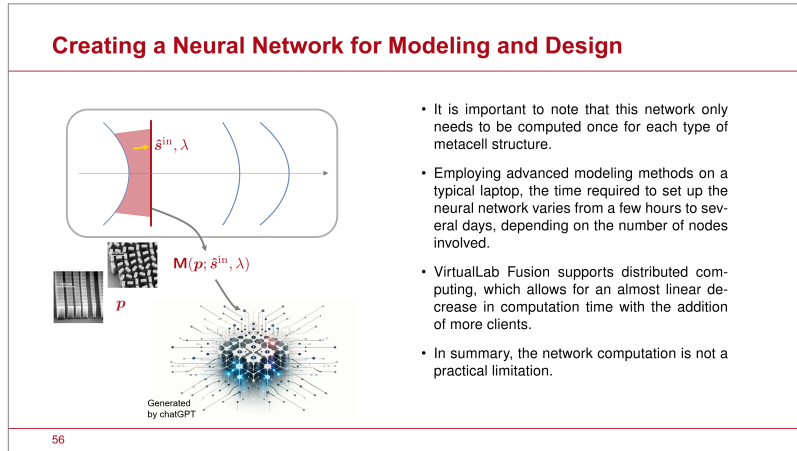


Figure 7: Slide #56

and design, it is essential to develop a robust method to calculate phase  $\Psi$  using  $\mathbf{M}U^{\text{in}}$ .

### Slides #54–55

The essential factors that define  $\mathbf{M}$ , and consequently the wavefront phase response  $\Psi$ , include the local structure defined by the parameter vector  $\mathbf{p}$ , here for two types of metacells, the direction of local incidence  $\hat{\mathbf{s}}^{\text{in}}$ , and the wavelength  $\lambda$ . It is important to highlight that in both physical and geometrical optics, the local direction vector is determined in an identical manner. To summarize our understanding of the dependencies of the matrix, we express the matrix as a function of the structural parameters, the local incidence direction vector, and the wavelength. Mathematically, the matrix's dependencies are denoted by  $\mathbf{M}(\mathbf{p}; \hat{\mathbf{s}}^{\text{in}}, \lambda)$ . In the realm of metalens modeling and design, possessing an in-depth understanding of the matrix values is absolutely paramount. This knowledge spans across the parameter space, the directional domain, and the wavelength range. We would like to highlight that any approach you encounter in the optics software sector that lacks the use of the full modeling matrix across necessary structure parameters, directions, and wavelength domains is not adequately advanced to provide the essential tools for investigating the potential of flat optics in your applications. Therefore, we compute all matrix values  $\mathbf{M}(\mathbf{p}; \hat{\mathbf{s}}^{\text{in}}, \lambda)$  in the parameter space for a chosen type of metacell structure, the pertinent direction domain, and the applied wavelength range. These matrix values function as nodes within a neural network, connecting the parameter space, the directional domain, and the wavelength range. This neural network encapsulates all the modeling and design data for a metalens with a specific metacell configuration.

### Slide #56

It is important to note that this network needs only to be computed once for each type of metacell structure. Employing advanced modeling methods on a typical laptop, the time required to set up the neural network varies from a few hours to several days,

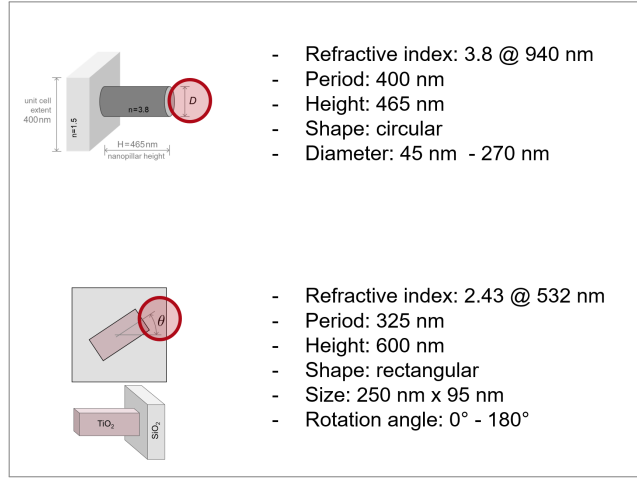


Figure 8: Structure specifications of metacells for example calculations. See also slide #58

depending on the number of nodes involved. VirtualLab Fusion supports distributed computing, which allows for an almost linear decrease in computation time with the addition of more clients. In summary, the network computation is not a practical limitation in flat optics modeling and design. Going forward, we will operate under the assumption that the network is already established and prepared to furnish all necessary details regarding the matrix elements.

### Slide #57

With the network established, we now address the task of determining the wavefront phase response  $\Psi$  of a metalens. First, we must grasp the essence of the task before us. For clarity, the discussion will focus on a single wavelength. Given a particular  $\mathbf{U}^{\text{in}}$ , the network supplies the magnitudes

$$|\{\mathbf{M}(\mathbf{p}; \hat{\mathbf{s}}^{\text{in}})\mathbf{U}^{\text{in}}\}_x| \text{ and } |\{\mathbf{M}(\mathbf{p}; \hat{\mathbf{s}}^{\text{in}})\mathbf{U}^{\text{in}}\}_y| \quad (9)$$

and the phases

$$\arg \{\mathbf{M}(\mathbf{p}; \hat{\mathbf{s}}^{\text{in}})\mathbf{U}^{\text{in}}\}_x \text{ and } \arg \{\mathbf{M}(\mathbf{p}; \hat{\mathbf{s}}^{\text{in}})\mathbf{U}^{\text{in}}\}_y. \quad (10)$$

### Slides #58–62

Next, we examine multiple scenarios in which we utilize two types of metacells based on the specifications in Fig. 8, along with different input polarizations. In this initial example, illustrated in Fig. 9, we use linearly polarized light to evaluate the amplitude results for the pillar metacell and the nanofin metacell, each characterized by different structural parameters. Figure 11 depicts the phases. The results for the nanofin structure reveal significant differences between the x and y components, unlike those observed in the pillar cell. Next, we alter the incident light from linear to circular polarization and examine the resulting amplitudes and phases. The results

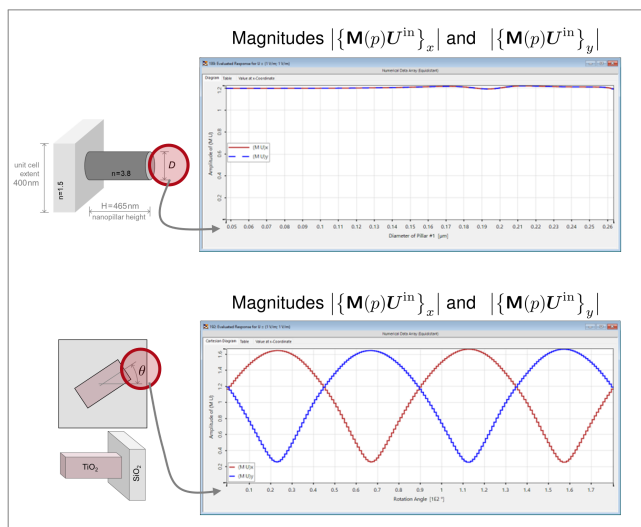


Figure 9: This illustration shows the variation in the **magnitudes of the x- and y-components** of the field following its interaction with the metacell on the left. The variation occurs by varying the structural parameter throughout its specified range. The input vector for the field is  $\mathbf{U}^{\text{in}} = (1, 1)^T$ , representing **linearly polarized** light, while the initial direction is  $\hat{\mathbf{s}}^{\text{in}} = 0$ . Structure specifications of metacells for example calculations. See also slide #59

are shown in Fig. 11 and 12. The phase value curves for the x- and y-components of both metacell types seem to be mainly shifted but otherwise remain similar or almost identical. The data presented in Figs. 9-12 suggest that accounting for the polarization effects in metacells is generally essential. This raises the question of deciding which phase should be recognized and handled as the wavefront phase response  $\Psi$ . The x- and y-components are two clear options. However, what should be done if they differ?

### Slides #63–65

From a mathematical perspective, we must choose a suitable candidate  $\Psi^{\text{c.c.}}$  for the wavefront phase response and extract it from the outcome of the matrix multiplication  $\mathbf{M}(\mathbf{p}; \hat{\mathbf{s}}^{\text{in}})\mathbf{U}^{\text{in}}$ . As a result, we obtain the residual phase components

$$\Delta\psi_{\ell}(\mathbf{p}) := \arg \{ \mathbf{M}(\mathbf{p}; \hat{\mathbf{s}}^{\text{in}}) \mathbf{U}^{\text{in}} \}_{\ell} - \Psi^{\text{c.d.}} \quad (11)$$

where  $\ell = x, y$ . The candidate's quality should be assessed based on the residual phase left, taking into account the magnitudes of the components. Without delving into the detailed definition, it is sufficient to state that we use a secondary momentum criterion on the phase residuals to evaluate the quality of a candidate. The quality measure is represented by a single value, denoted as  $\sigma^2$ . Figure 13 provides the metric values for the examples shown before. This table presents the  $\sigma^2$  values for the previously discussed examples, utilizing the phase of either the x- or y-component from the result of the matrix multiplication as the wavefront phase candidate. The

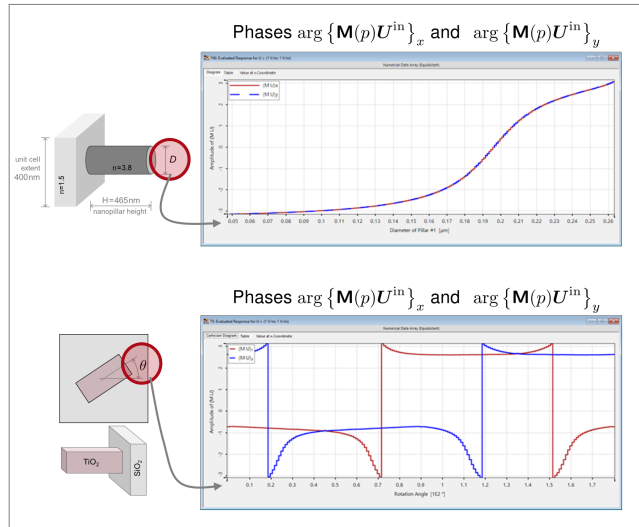


Figure 10: This illustration shows the variation in the **phases of the x- and y-components** of the field following its interaction with the metacell on the left. The variation occurs by varying the structural parameter throughout its specified range. The input vector for the field is  $\mathbf{U}^{\text{in}} = (1, i)^T$ , representing **linearly polarized** light, while the initial direction is  $\hat{\mathbf{s}}^{\text{in}} = 0$ . See also slide #60

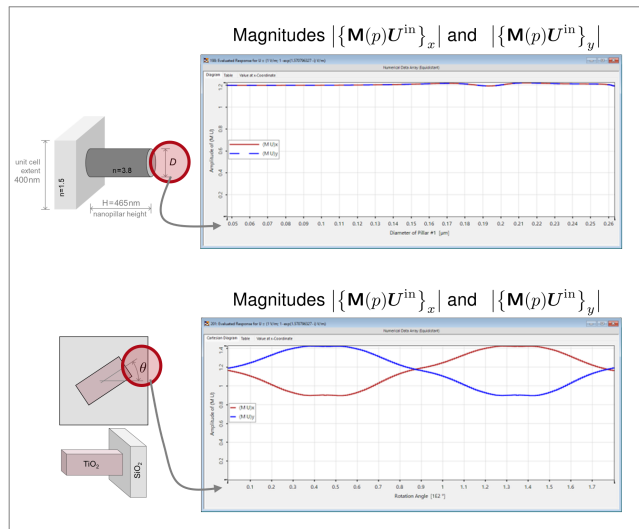


Figure 11: This illustration shows the variation in the **magnitudes of the x- and y-components** of the field following its interaction with the metacell on the left. The variation occurs by varying the structural parameter throughout its specified range. The input vector for the field is  $\mathbf{U}^{\text{in}} = (1, i)^T$ , representing **circularly polarized** light, while the initial direction is  $\hat{\mathbf{s}}^{\text{in}} = 0$ . Structure specifications of metacells for example calculations. See also slide #61

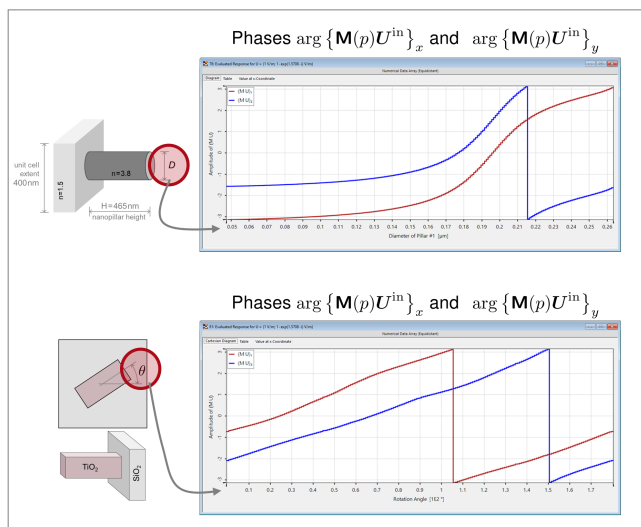


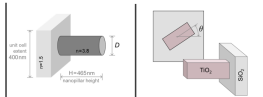
Figure 12: This illustration shows the variation in the **phases of the x- and y-components** of the field following its interaction with the metacell on the left. The variation occurs by varying the structural parameter throughout its specified range. The input vector for the field is  $\mathbf{U}^{\text{in}} = (1, 1)^T$ , representing **circularly polarized** light, while the initial direction is  $\hat{\mathbf{s}}^{\text{in}} = 0$ . See also slide #62

$\sigma^2$  values clearly demonstrate the significant polarization dependence of the nanofin structure. It is evident that in the case of linear polarization, both candidates are inadequate for nanofin metacells, and without a suitable wavefront phase, designing the metalens is unfeasible! This outcome emphatically illustrates that the straightforward method of choosing the wavefront phase as either the  $x$ - or the  $y$ -component from the matrix multiplication result  $\mathbf{M}(p; \hat{\mathbf{s}}^{\text{in}})\mathbf{U}^{\text{in}}$  is inadequate for the design and modeling of metalenses in any serious software development endeavor. This simplistic approach falls short of providing a robust and reliable foundation, highlighting the necessity for more sophisticated and nuanced methods to achieve viable and effective metalens modeling and designs. Consequently, we propose a technique for the design and simulation of metalenses that fully leverages the capabilities of the established neural network.

### Slides #66-67

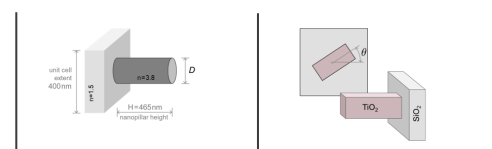
It is important to recall that the nodes in the network are represented by the matrix values, which are computed based on a selected metacell geometry and parameter space. To perform this computation, an appropriate simulation model needs to be utilized. Given that each meta-atom is surrounded by neighboring meta-atoms, the matrix analysis is conducted not on a single, isolated meta-atom, but rather on a meta-atom that is replicated periodically. This leads to the formation of a sub-wavelength grating, where the metacell serves as the periodic unit for analysis. The analysis of this **metacell grating** employs the Fourier Modal Method (FMM), also known as RCWA. We call this effective technique the Periodic Cell Approximation

**Values for the metric  $\sigma^2$**



$\Psi^{\text{c.d.}} = \arg \{ \mathbf{M}(p) \mathbf{U}^{\text{in}} \}_\ell$ for $\ell = x, y$	$x$	$y$	$x$	$y$
$\sigma^2$ for $\mathbf{U}^{\text{in}} = (1, 1)^T$	0	0	2.9	2.9
$\sigma^2$ for $\mathbf{U}^{\text{in}} = (1, i)^T$	0	0	0.04	0.04

Figure 13: The table displays the  $\sigma^2$  values, utilized for assessing the phase response quality. Lower values indicate better performance compared to higher values. Refer also to slide #66.



$\mathbf{W}_1 = (1, 0)^T$ $\mathbf{W}_2 = (0, 1)^T$	$\mathbf{W}_1 = (1, i)^T$ $\mathbf{W}_2 = (1, -i)^T$
--	---

Figure 14: The table reveals the vector bases for the two metacell configurations, derived from training the neural network. Refer also to slide #69.

(PCA). In Sections 7 and 8, we examine the precision of PCA and demonstrate ways to advance the simulation of a metastructure to set up the neural network. In the following discourse of this section, we employ the PCA method; however, all discussions and conclusions hold true even if we opt for an alternative approach.

### Slides #68–69

In the subsequent step, we train the network to identify an orthogonal vector basis  $\mathbf{W}_1$  and  $\mathbf{W}_2$ , which yields the optimal wavefront phase candidates  $\Psi_1^{\text{c.d.}}$  and  $\Psi_2^{\text{c.d.}}$  by minimizing  $\sigma^2$ . Upon completion of neural network training, the mode and phase candidate outcomes are embedded within the network, making it ready for application. Training of the network for our two example structures reveals the orthogonal bases shown in Table 14. As software developers, it is crucial for us that this neural network training concept provides a fully automated technology. It allows any user to choose one or more metacell geometries and initiate the training process, which produces everything required for successful metalens modeling and design.

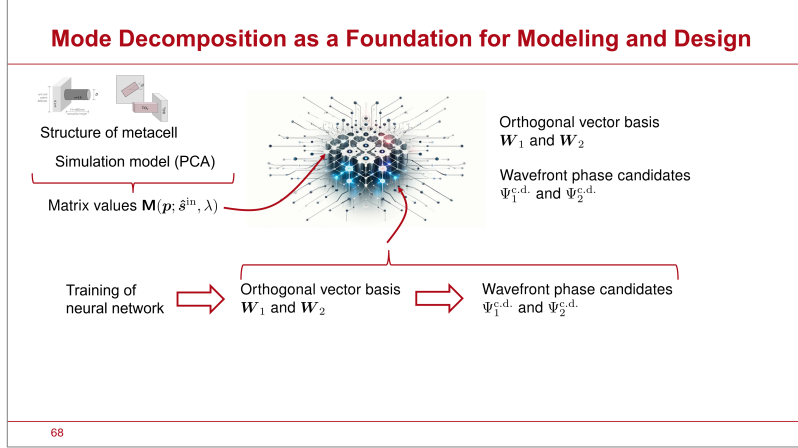


Figure 15: Slide #68

### Slide #70

To transmit the incident light through the metacell, the initial field is first decomposed into the modes supplied by the network, and we obtain

$$\begin{aligned} \mathbf{E}^{\text{in}} &= \mathbf{U}^{\text{in}} \exp[i\psi^{\text{in}}] \\ &= \{V_1^{\text{in}} \mathbf{W}_1 + V_2^{\text{in}} \mathbf{W}_2\} \exp[i\psi^{\text{in}}]. \end{aligned} \quad (12)$$

The network training has already resolved the modeling for both modes, allowing us to derive the output field:

$$\begin{aligned} \mathbf{E}^{\text{out}} &= \mathbf{U}_1^{\text{out}} \exp[i\{\psi^{\text{in}} + \Psi_1\}] + \mathbf{U}_2^{\text{out}} \exp[i\{\psi^{\text{in}} + \Psi_2\}] \\ &= \mathbf{U}^{\text{out}} \exp[i\{\psi^{\text{in}} + \Psi\}], \text{ if } \Psi_1 = \Psi_2 =: \Psi \end{aligned} \quad (13)$$

Typically, this field is composed of two modes; however, when the polarization dependency is minimal, the phases may align, allowing a single mode to adequately represent the output field. The potential presence of two modes in metacell modeling is not surprising. This phenomenon is also observed in birefringent media. The polarization effects observed for nanostructured surfaces, even when fabricated in isotropic media, are also referred to as form birefringence[1].

### Slides #71–72

In Eq. 13, the candidate notation is deliberately left out, as there remains a noticeable distinction between the wavefront responses represented in Eq. 13 and those provided by the neural network. The phases  $\Psi_j^{\text{c.d.}}(\boldsymbol{\rho})$  are not yet in the form of a wavefront phase, since they are in the form of  $2\pi$ -modulo. In addition, they may include some contributions which do not belong to a smooth wavefront phase, e.g., because they cannot be unwrapped like a phase vortex, as it is shown in Fig. 16. Thus, in a final step, the phase  $\Psi_j^{\text{c.d.}}(\boldsymbol{\rho})$  is unwrapped and filtered. We refer to this operation as  $\Theta$  and obtain

$$\left(\Theta\{\Psi_j^{\text{c.d.}} \bmod 2\pi\}(\boldsymbol{\rho})\right) = \Psi_j(\boldsymbol{\rho}) + \Delta\Psi_j(\boldsymbol{\rho}; \Theta) \bmod 2\pi. \quad (14)$$

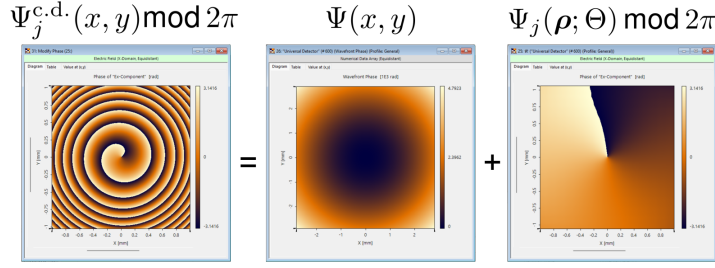


Figure 16: Example of the difference between the candidate phase and the resulting wavefront phase response. See also slide #71.

The method relies on spline interpolation techniques that were explored by Badar [5]. Through this unwrapping and filtering procedure, the output field for both modes  $j$  can be represented as

$$\mathbf{E}_j^{\text{out}}(\boldsymbol{\rho}) = \mathbf{U}_j^{\text{out}}(\boldsymbol{\rho}) \exp[i\psi^{\text{in}}(\boldsymbol{\rho}) + \Psi_j(\boldsymbol{\rho})], \quad (15)$$

with the smooth and unwrapped phase  $\psi^{\text{out}}(\boldsymbol{\rho}) = \psi^{\text{in}}(\boldsymbol{\rho}) + \Psi(\boldsymbol{\rho})$  and

$$\begin{aligned} \mathbf{U}_j^{\text{out}}(\boldsymbol{\rho}) &= \\ &= V_j(\boldsymbol{\rho}) \left( \begin{array}{l} \left\{ |(\mathbf{M} \mathbf{W}_j)_x|(\boldsymbol{\rho}) \right\} \exp[i\Delta\psi_{j,x}(\boldsymbol{\rho}) + i\Delta\Psi_j(\boldsymbol{\rho}; \Theta)] \\ \left\{ |(\mathbf{M} \mathbf{W}_j)_y|(\boldsymbol{\rho}) \right\} \exp[i\Delta\psi_{j,y}(\boldsymbol{\rho}) + i\Delta\Psi_j(\boldsymbol{\rho}; \Theta)] \end{array} \right). \end{aligned} \quad (16)$$

## 5 Design of Metalenses

### Slide #74

Next, we examine the creation of a metalens using the trained neural network as a foundation. The design is feasible for only one mode, provided that the modes have different wavefront phase responses. Thus, one of the two modes must be selected for the design. For this mode, the metalens is expected to generate a designated wavefront response  $\Psi(\boldsymbol{\rho})$ . Thus, initially this wavefront response must be selected. This can be achieved using various methods familiar in lens design, such as the configuration of a thin lens system. Alternatively, one could start by selecting a thick lens surface within a lens system that should be substituted with a metalens. In this scenario VirtualLab Fusion can determine the required wavefront phase response  $\Psi(\boldsymbol{\rho})$ .

The process of design can be entirely entrusted to the neural network, as it contains comprehensive details on the relationship between the produced phase value and the structural parameters within the metacell. During the design phase, the structural parameters for each metacell are determined depending on its lateral placement on the planar lens surface. In the concluding stage, the manufacturing data, for instance, in GSDII format, is generated.

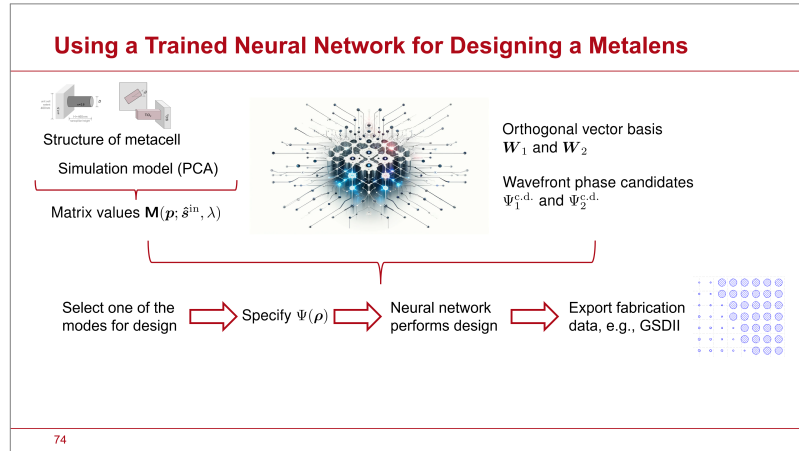


Figure 17: Slide #74

### Slide #75

The simulation and design techniques are incorporated into our proprietary Virtual-Lab Fusion software. These advanced techniques are planned to be released to the public in the upcoming 2025 software updates. In what follows, we would like to delve into some truly outstanding example demonstrations, which are done with our proprietary VirtualLab Fusion software.

## 6 Design Examples and Simulations

### Slide #77

We start with a pillar-type focusing metalens. Here, you can find the specifications along with a segment of the GDSII data for the lens. By employing the neural network, the lens design is completed within two seconds. Approximately 7500 by 7500 metacells are arranged across the lens, which has a diameter of three millimeters.

### Slide #78

The ray distribution within the system is obtained as one result of the multiscale simulation.

### Slides #79–82

The simulation also provides the magnitudes of the field and irradiances at the focal plane dependent on the polarization of the input field. In this example, as well as all subsequent ones, the simulation time ranges from approximately 10 seconds to less than a minute on a standard laptop. The PCA model estimates the efficiency to be around 94 percent. We will observe later in Sect. 7 that this estimate is somewhat overly optimistic.

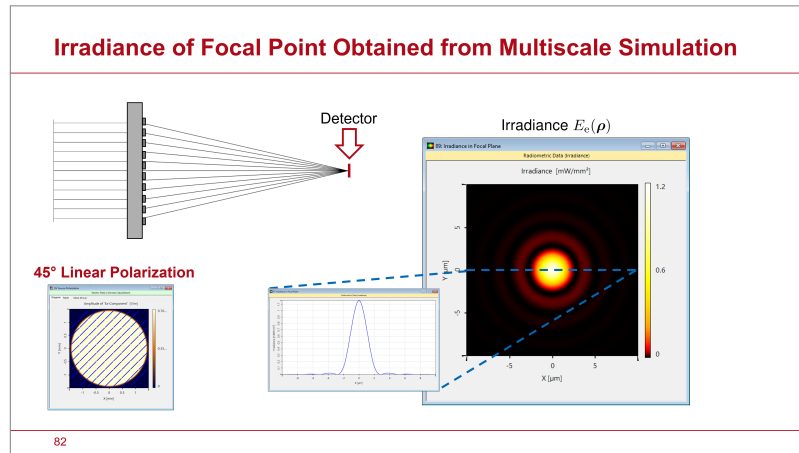


Figure 18: Slide #82

**Slides #83–84**

By carefully analyzing the wavefront phase response of the metalens using the neural network, we can also examine the aberrations caused by the metalens when using an off-axis input field.

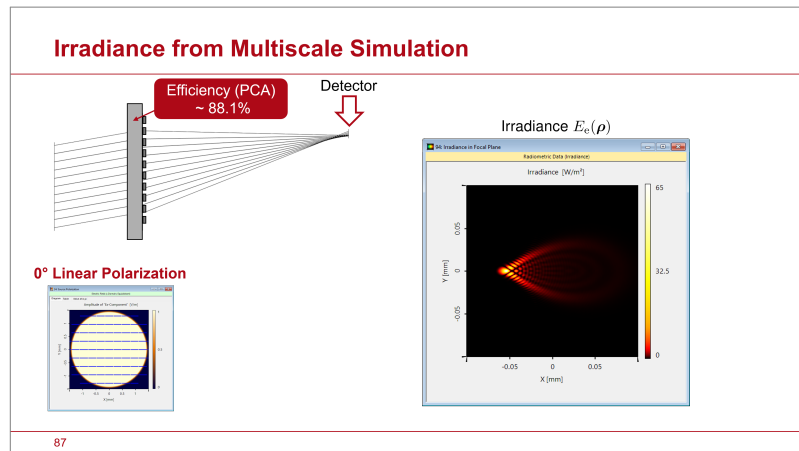


Figure 19: Slide #87

**Slides #85–88**

For the off-axis plane input field, the multiscale simulation provides the dot diagram, the field magnitudes, and the irradiance at the focal plane.

**Slides #89–94**

Next, we substitute the pillar-type metacell with a nanofin-type metacell. The design is done for one of the orthogonal modes, here for the right circularly polarized field. Then, similar simulations are performed as in case of the pillar-type cell. We obtain

ray distributions and the magnitudes after the lens. Due to high-frequency modulation, a Moire effect leads to a somewhat unusual appearance. A closer inspection uncovers the high-frequency modulation. This arises from the amplitude modulation across the parameter space, which we noted during our discussion on the neural network. The modulation causes a slight reduction in efficiency. The field magnitudes at the focal plane and the irradiance can also be readily calculated.

### Slides #95–96

We now switch the circular input polarization from right to left, and the impact on the ray distribution is clearly visible. The lens exhibits a divergent behavior! The calculation of the irradiance in the same plane as before confirms this result.

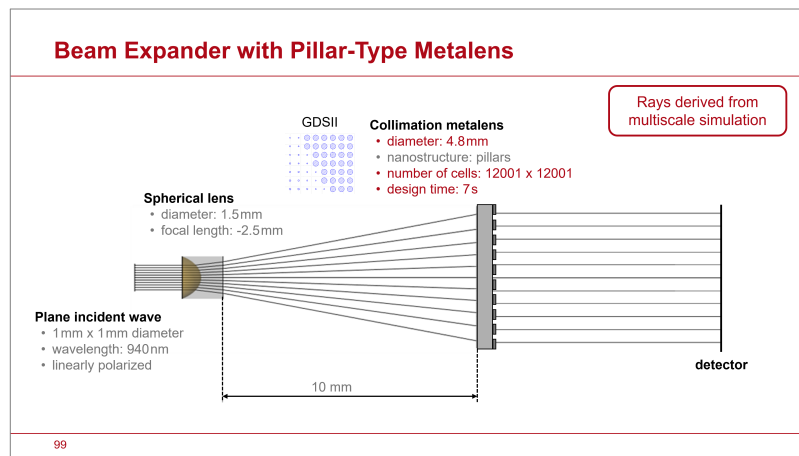


Figure 20: Slide #99

### Slides #97–101

In the next example, we substitute an aspherical lens surface in this beam expander setup with a pillar-type metalens. VirtualLab Fusion automatically determines the required phase response for the metalens after the surface to be replaced is selected. The metalens spans nearly 5 mm in diameter and comprises 12000 by 12000 metacells, ensuring its functionality. The trained neural network completes the design in 7 seconds. The performance of the metalens is showcased by the irradiance behind the lens and the calculated vectorial PSF.

### Slides #101–104

Concluding the simulation examples, we demonstrate a design in which the two modes of the nanofin metacell structure are utilized to create a bifocal lens system. We begin with a spherical lens positioned after the metalens. Then, the multiscale simulation approach provides ray results, which show clear spherical aberrations for both modes. This example demonstrates that our approach enables the incorporation of metalenses into optical lens systems, offering thorough access to aberration analysis.

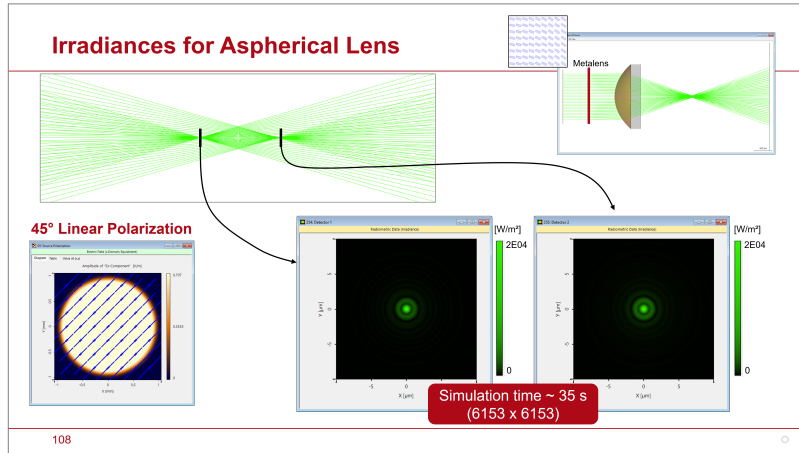


Figure 21: Slide #108

### Slides #105–109

Next, we design an appropriate aspherical lens and conduct the experiment again. For the mode with right circular polarization, the focal point is observed at the first detector location. When switched to the left circularly polarized mode, the focal point moved to the second position. When the input light is linearly polarized, both modes are produced in the output, resulting in two focal points. The metalens allows for the extra encoding of a phase dislocation, resulting in the irradiance dropping to zero at the center of the focal points.

The examples provided showcase the abilities of our advanced metalens technology, which we have developed and incorporated into VirtualLab Fusion, set for public release by 2025.

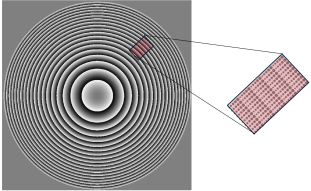
## 7 Limitations of the PCA Simulation Model and its Further Developments

### Slides #111–114

Next we take a closer, more critical examination of the Periodic Cell Approximation (PCA). In the PCA, it is assumed that neighboring metacells are identical. Practically, each metacell is encircled by additional metacells, which differ in structural parameters to varying degrees, thus interrupting the periodic cell condition to some extent. This situation arises particularly when a cycle of the lens zones is completed, causing the structural parameters to revert to their initial values. This results in discontinuities in the structure, leading to the production of additional stray light, a phenomenon that is also well recognized in diffractive lenses. Thus, the challenge lies in effectively integrating the neighboring metacells in a simulation model to more precisely represent the structural discontinuities. For such a model, it is crucial to account for the structural jumps. Simply including immediate neighbors is insufficient to improve accuracy. We propose using a **local metagrating approximation**

(LMGA), akin to the modeling of diffractive lenses. This method not only provides high computational efficiency, but also distinguishes the stray light from the desired light in additional orders. These extra orders have clearly defined wavefront phases. That enables the propagation of the light per order through the lens system, in addition to the intended light. This fact holds particular significance if a metalens is integrated into a lens system. Then it is crucial to assess the impact of stray light, characterized by additional orders, on the image plane, for instance, on the PSF.

**Local Metagrating Approximation (LMGA)**



- Thus, the challenge lies in effectively integrating the neighboring metacell in a simulation model to more precisely represent the structural discontinuities.
- We propose using a **local metagrating approximation**, akin to the modeling of diffractive lenses.
- This method not only provides high computational efficiency but also distinguishes the stray light from the desired light in additional orders.
- These extra orders have clearly defined wavefront phases, allowing them to propagate through the lens system together with the intended light.

114

Figure 22: Slide #114

### Slide #115

The rigorous Fourier Modal Method (FMM), also known as RCWA, is employed for analyzing the local gratings. The differences in results between PCA and LMGA can be systematically analyzed by generating metagratings with PCA and subsequently simulating them using both the rigorous Fourier Modal Method and PCA for comparison.

### Slides #116–129

We have carried out this procedure and obtained the results shown in Tab. 23 for the pillar-type metacells. We created metagratings with a period that decreases, expressed in the table as multiples of the wavelength. We also specify the maximum numerical aperture of the lens that can be designed with this period. Next, we present the efficiency of each grating in directing light into the intended order, contrasting the results obtained using PCA and FMM. Subsequently, we show the same analysis for the reflected light. In the final column, we present the efficiency of all higher transmitted orders as calculated using the FMM. We present a comparison of computed wavefront phase responses, showcasing results for both PCA and FMM as detailed in the slides. Consider the results starting with the largest period. The results obtained from PCA closely resemble those from FMM, although FMM exhibits a marginally lower efficiency. As anticipated, a slight phase deviation occurs at the structural discontinuity. Reducing the grating period further confirms that

Period/ Lambda	NA of Lens	Efficiency of Desired Order		Reflected light		Transmitted orders (FMM)
		PCA	FMM	PCA	FMM	
10.6	0.094	95.9 %	94.4 %	4.1 %	3.8 %	1.8 %
5.3	0.189	95.9 %	92.6 %	4.1 %	4.4 %	3 %
3.2	0.313	95.9 %	86.7 %	4.1 %	8.5 %	4.8 %
2.9	0.345	95.9 %	87.6 %	4.1 %	7.5 %	4.9 %
2.1	0.476	95.9 %	82.2 %	4.1 %	12.3 %	5.5 %
1.3	0.769	95.9 %	76.6 %	4.1 %	19.6 %	3.8 %

Figure 23: The table gives an overview of a comparing the diffraction efficiencies of metagratings, when analyzed with the PCA and the LMGA. The gratings are all designed using the PCA. Refer also to slides #117-129.

while PCA predicts phase values well, it does not effectively account for stray light in higher reflected and transmitted orders. When the grating period approaches the wavelength of light, entering the resonance domain, PCA becomes ineffective. The response becomes also highly polarization dependent. The resonance region of local gratings is unsuitable for lens design, thereby restricting the highest achievable numerical aperture of the lens.

**Using a Trained Neural Network for Modeling**

Structure of metacell

Simulation models:  
PCA and LMGA

Matrix values  $M(p, \hat{s}^{in}, \lambda)$



Orthogonal vector basis  
 $W_1$  and  $W_2$

Wavefront phase candidates  
 $\Psi_1^{c,d}$  and  $\Psi_2^{c,d}$

$$\begin{aligned}
 E^{in} &= U^{in} \exp[i\psi^{in}] \\
 &= \{V_1^{in} W_1 + V_2^{in} W_2\} \exp[i\psi^{in}] \quad \Rightarrow \quad E^{out} = U_1^{out} \exp[i\{\psi^{in} + \Psi_1\}] + U_2^{out} \exp[i\{\psi^{in} + \Psi_2\}] \\
 &= U^{out} \exp[i\{\psi^{in} + \Psi\}], \text{ if } \Psi_1 = \Psi_2 =: \Psi
 \end{aligned}$$

132

Figure 24: Slide #132

### Slides #130-132

We summarize the results:

- The PCA offers high precision in phase modeling and design outside of the resonance domain of local gratings.
- PCA is unable to forecast the emergence of stray light in higher-order reflections

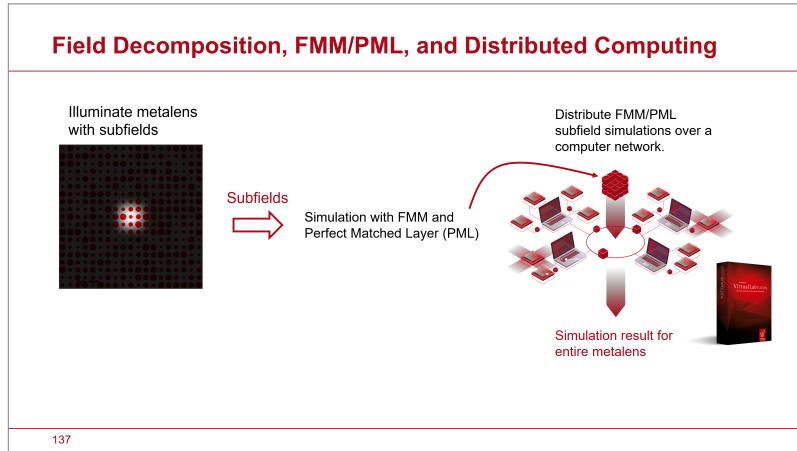


Figure 25: Slide #137

and transmissions.

- The Local Metagrating Approximation (LMGA) can achieve this.

We plan to integrate a tool into our VirtualLab Fusion software to conduct grating analyses similar to the previous example, applicable to metagratings regardless of the type of metacells used. This allows gaining a preliminary insight into the capabilities of the chosen metacell. In addition, we enhance the neural network by incorporating the Local Metagrating Approximation simulation model, allowing it to execute the extended modeling as well. The local grating approximation concept has been integrated into and utilized for diffractive lenses within VirtualLab Fusion.

## 8 “Roughness” of Metalenses

### Slides #135–137

At the conclusion of this article, we would like to provide a quick overview of our strategy to advance the model further. Integrating the PCA and LMGA simulation models into our neural network approach offers a commendable balance between accuracy and speed for simulating flat lenses within lens systems. Nevertheless, they do not completely consider the specific grid arrangement of the metacells. From a modeling standpoint, this phenomenon results in a slight increase in stray light, which can be interpreted as a consequence of the metalens’s intrinsic "roughness." We like to make the point, that this intrinsic roughness plays a similar role in metalens modeling as modeling the roughness and other defects of lens surfaces. We are working on solutions for both aspects, as the modeling challenges are closely connected. The centerpiece of the approach is the analysis of the scattering effect of the metalenses and rough surfaces. To achieve this, we have devised a Fourier Modal Method (FMM) in combination with Perfect Matched Layer (PML) that utilizes lateral decomposition of the incident field alongside distributed computing. In one of our recent releases

in 2024, VirtualLab Fusion has introduced distributed computing in a highly user-friendly manner. Combining the results of all clients in the computer network provides the simulated result of the entire metalens. This allows for a thorough investigation of the scattering impact of lens regions, with the area size being adjustable based on the number of clients in the distributed computing network.

We want to stress that, while analyzing the roughness and its impact on lens system performance is crucial, no lens designer will cease using available software tools to design lens systems simply because they are unsure how to incorporate roughness analysis into their designs. This pragmatic approach should also be applied to flat lenses, including metalenses. With VirtualLab Fusion, we offer an expanding range of tools and techniques for designing and simulating flat lenses with precision and efficiency, enabling you to explore their potential in your work.

## 9 Conclusion

### Slide #139

We would like to conclude this article by reiterating that flat lenses are a remarkable and exciting addition to the optical design toolkit, especially in the areas of imaging and illumination. Incorporating flat lens technology into lens design workflows is essential for comprehending and utilizing their full potential. In this article we have outlined our approach to addressing this challenging problem. Our approach to solving this task is facilitated by the remarkable multiscale simulation technology offered by VirtualLab Fusion. In the forthcoming software updates in 2025, we will be incorporating the flat lens technologies showcased in this article, allowing you to use them directly.

## References

- [1] M. Born and E. Wolf. *Principles of optics*. 6. Pergamon Press, New York, 1980.
- [2] P. Lalanne et al. “Design and fabrication of blazed binary diffractive elements with sampling periods smaller than the structural cutoff”. In: *J. Opt. Soc. Am. A* 16.5 (1999), pp. 1143–1156.
- [3] Mohammadreza Khorasaninejad et al. “Metalenses at visible wavelengths: Diffraction-limited focusing and subwavelength resolution imaging”. In: *Science* 352.6290 (June 3, 2016), pp. 1190–1194. ISSN: 0036-8075, 1095-9203. DOI: [10.1126/science.aaf6644](https://doi.org/10.1126/science.aaf6644). URL: <https://www.science.org/doi/10.1126/science.aaf6644> (visited on 11/15/2024).
- [4] Philippe Lalanne and Pierre Chavel. “Metalenses at visible wavelengths: past, present, perspectives”. In: *Laser & Photonics Reviews* 11.3 (May 2017), p. 1600295. ISSN: 1863-8880, 1863-8899. DOI: [10.1002/lpor.201600295](https://onlinelibrary.wiley.com/doi/10.1002/lpor.201600295). URL: <https://onlinelibrary.wiley.com/doi/10.1002/lpor.201600295> (visited on 11/15/2024).
- [5] Irfan Badar, Christian Hellmann, and Frank Wyrowski. “Wavefront phase representation by Zernike and spline models: a comparison”. In: *Journal of the Optical Society of America A* 38.8 (Aug. 1, 2021), p. 1178. ISSN: 1084-7529, 1520-8532. DOI: [10.1364/JOSAA.427519](https://doi.org/10.1364/JOSAA.427519). URL: <https://opg.optica.org/abstract.cfm?URI=josaa-38-8-1178> (visited on 09/22/2022).
- [6] Fan Yang et al. “Wide field-of-view metalens: a tutorial”. In: *Advanced Photonics* 5 (May 1, 2023). ADS Bibcode: 2023AdPho...5c3001Y, p. 033001. DOI: [10.1117/1.AP.5.3.033001](https://ui.adsabs.harvard.edu/abs/2023AdPho...5c3001Y). URL: <https://ui.adsabs.harvard.edu/abs/2023AdPho...5c3001Y> (visited on 11/15/2024).